

Seasonal Forecasts of Tropical Cyclones using GFDL SPEAR and HiFLOR-S

Hiroyuki Murakami¹, Thomas L. Delworth¹, Nathaniel C. Johnson¹,
Feiyu Lu^{1,2}, Colleen E. McHugh^{1,3}, and Liwei Jia¹

¹National Oceanic and Atmospheric Administration/Geophysical Fluid
Dynamics Laboratory, Princeton, NJ, USA

²University Corporation for Atmospheric Research, Boulder, CO, USA

³Science Applications International Corporation, Reston, VA, USA

Revised on October 29, 2024

Submitted to *Journal of Climate* on July 5, 2024

Abstract

1
2 The seasonal prediction skill of tropical cyclone (TC) activity is evaluated using the Seamless
3 System for Prediction and Earth System Research (SPEAR), a modeling system developed at
4 the Geophysical Fluid Dynamics Laboratory (GFDL) for experimental real-time seasonal
5 forecasts. Compared with previous GFDL seasonal prediction models, SPEAR demonstrates
6 improved skill in predicting TC activity for the western North Pacific, while exhibiting
7 comparable or slightly degraded skill for the eastern North Pacific and North Atlantic. These
8 changes in prediction skill do not always align with changes in prediction skill in large-scale
9 variables, particularly over the North Atlantic. This study highlights that changes in the
10 model's response of TCs to large-scale variables, as well as the changes in the amplitude of
11 interannual variations in TC genesis frequency, are crucial for the changes in TC prediction
12 skill. Using the predicted sea surface temperatures from SPEAR as lower boundary conditions,
13 the High-Resolution Forecast-Oriented Low Ocean Resolution model (HiFLOR-S) was
14 employed to predict intense TCs, demonstrating skillful predictions of major hurricanes that
15 are comparable to the previous HiFLOR coupled model predictions.

16

Significance Statement

17
18 This study reveals the prediction skill in seasonal forecasting of tropical cyclones using a new
19 experimental real-time seasonal prediction system developed at the Geophysical Fluid
20 Dynamics Laboratory. The new system demonstrates skillful prediction of tropical cyclones in
21 the western North Pacific, eastern North Pacific, and North Atlantic a few months before the
22 hurricane season, with notable differences in the skill compared to the previous prediction
23 system. The findings suggest that higher prediction skill in large-scale variables, such as
24 vertical wind shear and sea surface temperatures, do not necessarily lead to higher prediction
25 skill for tropical cyclones. This underscores that even when a model accurately predicts large-
26 scale variables, its predictions of tropical cyclones could still be inaccurate. Our findings
27 emphasize the need to refine the model's response of tropical cyclones to specific large-scale
28 environments, rather than focusing only on improving large-scale environment predictions, to
29 enhance the accuracy of dynamical seasonal predictions for tropical cyclones.

30

31 1. Introduction

32 Tropical cyclones (TCs), defined as storms with a maximum wind speed of $\geq 17.5 \text{ m s}^{-1}$,
33 are the costliest natural disasters worldwide, making the prediction of TC activity on a
34 seasonal time scale of vital socio-economic interest. Since Gray (1984a, b), numerous studies
35 have attempted to develop seasonal TC predictions. Comprehensive reviews of seasonal TC
36 predictions over the past 40 years are available in Camargo et al. (2007), Klotzbach et al.
37 (2019), and Chu and Murakami (2022). Specifically, dynamical seasonal TC predictions began
38 in 2001 at the European Centre for Medium-Range Weather Forecasts (ECMWF) (Vitart and
39 Stockdale 2001). Since then, many dynamical models have demonstrated skillful predictions
40 of TC activity a few months in advance from the storm season, specifically over the North
41 Atlantic (NA) (e.g., LaRow et al., 2008; Zhao et al., 2010; Chen et al., 2011 and 2013; Camp
42 et al., 2015; Befort et al., 2022).

43 However, most seasonal predictions have focused on forecasting TC activity based on
44 basin-wide statistics, such as the basin-total frequency of named storms (with a maximum
45 wind speed $\geq 17.5 \text{ m s}^{-1}$), hurricanes (with a maximum wind speed $\geq 34.0 \text{ m s}^{-1}$), major
46 hurricanes (with a maximum speed $\geq 49.4 \text{ m s}^{-1}$), and Accumulated Cyclone Energy (ACE;
47 Bell et al., 2000) (Klotzbach et al., 2019; Takaya et al., 2023). These basin-wide variables have
48 also been the targets for predicting seasonal hurricane outlooks produced by the National
49 Oceanic and Atmospheric Administration (NOAA) (Klotzbach et al., 2019). However, the
50 World Meteorological Organization (WMO) has suggested exploring beyond the predictions
51 of basin-wide statistics, such as sub-basin scale information like landfalling TCs, which are
52 more relevant to society and stakeholders (Klotzbach et al., 2019; Takaya et al., 2023).

53 The NOAA Geophysical Fluid Dynamics Laboratory (GFDL) is one of the U.S.
54 research institutions contributing to the North American Multi-Model Ensemble Project
55 (NMME; Kirtman et al., 2014). Among the NMME models, GFDL models incorporate the
56 highest horizontal resolution (i.e., 50-km mesh), enabling direct prediction of TCs. These real-
57 time and retrospective TC predictions from GFDL have been shared with the experts at the
58 NOAA Climate Prediction Center (CPC) and the National Hurricane Center (NHC),
59 supporting their seasonal hurricane outlook, issued each May and updated in August.
60 Previously, GFDL had used the Forecast-oriented Low Ocean Resolution of GFDL Coupled
61 Model version 2.5 (FLOR; Vecchi et al., 2014) and the high-resolution version of FLOR

62 (HiFLOR) (Murakami et al., 2015, 2016a) for real-time TC predictions. Both FLOR and
63 HiFLOR showed reasonable skill not only for basin-wide named storms, major hurricanes, and
64 ACE, but also for regional TC frequency of occurrence (Vecchi et al., 2014; Murakami et al.,
65 2016a,b; Zhang et al., 2017; G. Zhang et al., 2019), TC rainfall (W. Zhang et al., 2019), and
66 extratropical transition of TCs (Liu et al., 2018).

67 In January 2021, GFDL upgraded its real-time experimental seasonal to decadal
68 prediction system to Seamless System for Prediction and Earth System Research (SPEAR;
69 Delworth et al., 2020; Lu et al., 2020), replacing FLOR. The predictions from the new SPEAR
70 system demonstrated good skill in predicting climate variability, such as ENSO (Lu et al.,
71 2020), and hydroclimate extremes, including heatwaves (Jia et al., 2022), atmospheric rivers
72 (Tseng et al., 2021), Arctic and Antarctic sea ice (Bushuk et al., 2021, 2022), and wintertime
73 temperature swings (Yang et al., 2022). While SPEAR was not specifically optimized for
74 improving TC predictions relative to FLOR, the prediction skill of seasonal TC activity by
75 SPEAR has not been investigated or reported previously.

76 In this study, we assess the prediction skill of TCs using SPEAR and compare these
77 evaluations with those from previous GFDL prediction models, FLOR and HiFLOR. The
78 predictions target seasonal mean TC activities, including basin-total TC genesis frequency for
79 different storm intensity categories, Accumulated Cyclone Energy (ACE), and Power
80 dissipation Index (PDI), as well as regional TC occurrence and landfalling frequencies in the
81 western North Pacific (WNP), eastern North Pacific (ENP), and North Atlantic (NA) basins
82 (see Fig. 3 in Murakami et al., 2015 for regional boundaries). Additionally, we demonstrate
83 prediction skill through HiFLOR downscaling from SPEAR's predicted sea surface
84 temperatures (SSTs). Furthermore, we examine the causes of differences in prediction skill for
85 TC variables between the new and previous prediction models, particularly in relation to
86 changes in the skill of large-scale variables. A unique case from the 2023 predictions is also
87 presented, in which the two models in the new prediction system provided differing
88 predictions for the hurricane season, with possible reasons for these discrepancies explored.
89 Section 2 describes the methods, including models, seasonal predictions, TC detection method,
90 observed datasets, and forecast skill metrics. Section 3 presents the results, with a summary
91 provided in Section 4.

92

93 2. Methods

94 *a. Dynamical Models*

95 The dynamical models used in this study include FLOR (Vecchi et al., 2014), HiFLOR
96 (Murakami et al., 2015, 2016a), and SPEAR (Delworth et al., 2020), all developed at GFDL.
97 FLOR comprises 50-km mesh atmosphere and land components coupled with 100-km mesh
98 sea ice and ocean components. The atmosphere and land components are adapted from the
99 Coupled Model version 2.5 (CM2.5; Delworth et al., 2012), while the sea ice and ocean
100 components are derived from the Coupled Model version 2.1 (CM2.1; Delworth et al., 2006).
101 HiFLOR is nearly identical to FLOR, except for the horizontal resolution of the atmosphere
102 and land components, which employs a 25-km mesh, along with some minor adjustments in
103 parameters in the dynamical core and physical parameterizations (Murakami et al., 2015;
104 Vecchi et al., 2019).

105 The GFDL SPEAR incorporates a coupled atmospheric-oceanic model consisting of
106 the new AM4-LM4 atmosphere and land-surface model (Zhao et al., 2018), coupled with the
107 MOM6 ocean model and SIS2 sea-ice model (Adcroft et al., 2019). Similar to FLOR, SPEAR
108 employs a 50-km mesh for the atmosphere and land components and a 100-km mesh for sea
109 ice and oceanic components.

110

111 *b. Retrospective Seasonal Predictions*

112 For each year and month from 1992 to 2020, 12-month retrospective seasonal
113 predictions were generated by initializing each model to observationally constrained
114 conditions for the ocean and sea ice components (Vecchi et al., 2014; Murakami et al., 2015,
115 2016; Lu et al., 2020). A summary of the seasonal predictions is provided in Table 1.

116

117 **Table 1** Prediction configurations. For each previous prediction system (i.e., FLOR and
118 HiFLOR) and new prediction system (i.e., SPEAR and HiFLOR-S), the following are listed:
119 horizontal resolution of atmosphere and land components; horizontal resolution of ocean and
120 sea-ice components; number of ensemble members for the predictions; methods to generate
121 ocean initial conditions; methods to generate atmosphere and land initial conditions; period for
122 retrospective predictions; initial months; methods for ocean bias adjustments during forecasts;
123 and reference for the model and predictions.

	Previous Prediction System		New Prediction System	
	FLOR	HiFLOR	SPEAR	HiFLOR-S
Atmosphere and land resolution	50 km	25 km	50 km	25 km
Ocean and sea-ice resolution	100 km	100 km	100 km	100 km
Ensemble member	12	12	15	15
Ocean IC	ECDA (Zhang and Rosati, 2010)	ECDA (Zhang and Rosati, 2010)	SPEAR_ECDA (Lu et al., 2020)	N/A
Sea ice IC	ECDA (Zhang and Rosati, 2010)	ECDA (Zhang and Rosati, 2010)	SPEAR nudged (Lu et al. 2020)	N/A
Atmosphere and land IC	SST-forced AMIP simulaitons	SST-forced AMIP simulaitons	SPEAR nudged (Lu et al. 2020)	SST-forced AMIP simulaitons
Initial years	1992-2020	1992-2020	1992-2020	1992-2020
Initial months	Each month of January-December	January, April, June, July	Each month of January-December	April, May, July
Ocean adjustment during forecasts	Flux adjustment (Vecchi et al. 2014)	N/A	OTA (Lu et al. 2020)	Nudged to the SPEAR predicted SST
Reference	Vecchi et al.(2014)	Murakami et al. (2015,2016)	Lu et al. (2020)	N/A

124

125

126

For the FLOR and HiFLOR predictions, the 12-member initial conditions for the ocean and sea ice were generated using the GFDL’s ensemble coupled data assimilation system (ECDA; Zhang and Rosati 2010; Chang et al., 2013). The atmosphere and land components were initialized from a suite of SST-forced atmosphere-land-only simulations (Vecchi et al., 2014). HiFLOR provides forecasts initialized on the first day of the month only from July, June, April, and January, whereas FLOR offers forecasts starting every month. To mitigate climatological biases in SSTs and the associated model drift with increasing lead time, seasonal predictions by FLOR were conducted using “flux adjustment”, which adjusts the model’s air-sea fluxes of momentum, enthalpy, and freshwater to align the long-term climatology of SST and surface wind stress with the observations (Vecchi et al., 2014). HiFLOR predictions do not apply flux adjustment.

137

For the SPEAR predictions, the 15-member initial ocean conditions were generated with SPEAR_ECDA (Lu et al., 2020). The atmosphere and land components, as well as the sea ice component for SPEAR, were initialized from restoring simulations, where the SSTs were nudged to the values of Optimum Interpolation Sea Surface Temperature (OISST, Reynolds et al., 2002). The SPEAR predictions incorporate ocean tendency adjustment (OTA; Lu et al., 2020) to reduce three-dimensional oceanic biases, improving SST climatology and variability.

144

To complement SPEAR for intense TC predictions, we conducted HiFLOR predictions forced with the predicted SSTs by SPEAR (HiFLOR-S). These HiFLOR-S predictions were not initialized with data assimilation experiments, although simulated SSTs were nudged to SPEAR-predicted SSTs at a 5-day time scale. The initial conditions of ocean and sea ice components for HiFLOR-S were derived from an arbitrary year in a HiFLOR long-term control climate simulation. For example, ensemble member 1 is initiated from the restart file of year 101, while ensemble member 2 is initiated from that of year 111. However, our

150

151 preliminary assessment revealed that the choice of years has little impact on the results of TC
152 predictions, as prescribing SSTs from the SPEAR-predicted values is more critical for TC
153 predictions than the differences in ocean initial conditions. Meanwhile, the atmosphere and
154 land initial conditions were derived from the SST nudged experiments in which the SSTs were
155 nudged to the values of OISST.

156 We primarily compare the predictions of TC activity in the WNP, ENP, and NA in the
157 boreal summer and early fall season (i.e., July–November). Forecasts initialized in July
158 (January) are defined as lead-month 0 or L0 (6 or L6) forecasts. Since the retrospective
159 predictions by FLOR and HiFLOR are only available for the period 1992–2020, we compare
160 these predictions with the predictions by SPEAR and HiFLOR-S over the same period. Given
161 the limited computational resources, retrospective predictions are only available for L0, L2,
162 and L3 for HiFLOR-S, and L0, L1, L2, L5, and L6 for HiFLOR, although retrospective
163 predictions are available for every initial month between L0 and L6 for SPEAR and FLOR.
164 Additional prediction differences for the summer of 2023 will be shown for SPEAR and
165 HiFLOR-S in Section 3. c.

166 Vecchi et al. (2014) revealed that the prediction skill in the basin-wide frequency of
167 hurricanes in the NA by FLOR showed comparable or higher prediction skill compared with
168 other state-of-the-art prediction systems (e.g., Vitart et al., 2007; Klotzbach and Gray 2009;
169 Zhao et al., 2010; LaRow et al., 2010; Wang et al., 2009; Chen and Lin 2013; see Fig.9 in
170 Vecchi et al., 2014). Therefore, the prediction skill of FLOR can serve as a reference for
171 typical skill obtained by dynamical TC seasonal predictions. As also noted by Befort et al.
172 (2022), prediction skill for TC activity is relatively higher in the NA than in other ocean basins
173 like the WNP and ENP for most of the dynamical model predictions.

174

175 *c. TC Detection Method*

176 The detection of model-generated TCs followed the method outlined by Harris et al.
177 (2016) and Murakami et al. (2015). Briefly, the tracking scheme employs the flood fill
178 algorithm to identify closed contours of a specified negative sea level pressure (SLP) anomaly
179 with a warm core (temperature anomaly higher than 1K for FLOR and SPEAR and 2K for
180 HiFLOR and HiFLOR-S). Additionally, the detection scheme requires that a TC must persist
181 for at least 36 hours while maintaining its warm core, along with meeting a specified surface

182 wind speed criterion (15.75 m s^{-1} for FLOR and SPEAR and 17.5 m s^{-1} for HiFLOR and
183 HiFLOR-S). These thresholds were determined by the previous studies of FLOR and HiFLOR
184 (Murakami et al. 2015). Because the horizontal resolution of FLOR and SPEAR is 50-km
185 mesh and unable to represent intense TCs, the warm core and wind speed threshold were
186 relaxed from those for HiFLOR and HiFLOR-S as in the previous studies (Murakami et al.
187 2015).

188

189 *d. Observational Datasets and Large-scale Variables*

190 The observed TC “best-track” data for the period 1992–2023 were obtained from the
191 International Best Track Archive for Climate Stewardship (IBTrACS v04r00) (Knapp et al.,
192 2010). We use a compilation from the NHC and Joint Typhoon Warning Center (JTWC),
193 identified by the flag ‘usa’ in the IBTrACS dataset. We considered TCs with tropical storm
194 intensities or stronger, defined as TCs possessing 1-minute sustained surface winds of 17.5 m
195 s^{-1} or greater.

196 We utilized the OISST (Reynolds et al., 2002) and the Japanese 55-year Reanalysis
197 (JRA-55) (Kobayashi et al., 2015) for the period 1992–2023 as observed SST and atmospheric
198 large-scale variables, respectively. To elucidate the factors contributing to the differences in
199 the prediction skill in TCs among the GFDL models, we compared the prediction skill in key
200 large-scale variables. These large-scale variables include vertical wind shear between 850hPa
201 and 200 hPa (V_s), relative humidity at 600 hPa (RH_{600}), absolute vorticity at 850 hPa (ζ_{a850}),
202 Maximum Potential Intensity (MPI ; Bister and Emanuel, 1998), vertical motion at 500 hPa
203 (ω_{500}), shear vorticity of zonal winds at 500 hPa (U_{y500}), and SST anomaly (SST), which are
204 commonly used for tropical cyclone genesis potential indices (e.g., Emanuel and Nolan, 2004;
205 Murakami and Wang, 2010; Wang and Murakami, 2020; Murakami and Wang, 2022). Here,
206 anomalies are defined as the deviations from the mean climatology of 1992–2020, with
207 climatology calculated separately for each lead month prediction. These large-scale variables
208 were evaluated exclusively over the main development region of TCs for each WNP (10–
209 25°N , $110\text{--}150^\circ\text{E}$), NA ($10\text{--}25^\circ\text{N}$, $80\text{--}20^\circ\text{W}$), and ENP ($5\text{--}25^\circ\text{N}$, $130\text{--}100^\circ\text{W}$) ocean basin.

210

211 *e. Metrics for Evaluation of Forecast Skill*

212 As in Murakami et al., (2016a), storms are classified into three categories based on
 213 their lifetime maximum intensity: Tropical Storms (TCS; $\geq 17.5 \text{ m s}^{-1}$); Hurricanes (HUR;
 214 $\geq 32.9 \text{ m s}^{-1}$); and Category 3–5 (or major) hurricanes (C345; $\geq 49.4 \text{ m s}^{-1}$). We note that while
 215 a hurricane is referred to as a “typhoon” in the WNP, we use the term “hurricanes” for WNP
 216 typhoons in this study. Additionally, we considered ACE, defined as the sum of the square of
 217 the maximum surface wind velocity throughout the lifetime of a TC, normalized by a factor of
 218 10^5 ($10^5 \text{ m}^2 \text{ s}^{-2}$; Bell et al., 2000). Along with ACE, we evaluated PDI, which is similarly
 219 defined, but as the sum of the cube of the maximum surface wind velocity throughout the
 220 lifetime of a TC, normalized by a factor of 10^7 ($10^7 \text{ m}^3 \text{ s}^{-3}$; Emanuel, 2005, 2007). We
 221 examined the prediction skill in interannual variation of the basin-wide frequencies for TCS,
 222 HUR, C345, ACE, PDI, and the landfalling TCs over the Continental U.S. (US), Caribbean
 223 Islands (CAR), and Hawaiian Islands (HI).

224 As outlined in Murakami et al. (2016a), we employed two scores to assess prediction
 225 skill for the TC activity relative to observed values: Spearman’s rank correlation coefficient
 226 (RCOR) and mean square skill score (MSSS) (Kim et al., 2012; Li et al., 2013). Following
 227 Vecchi et al. (2014), we chose Spearman’s rank correlation instead of Pearson’s correlation as
 228 our correlation metric because we do not expect the ensemble-mean forecasts of TC counts
 229 and the observed annual TC counts (integer values) to follow a Gaussian distribution.
 230 Additionally, Pearson’s correlation is sensitive to outliers, which are common in TC data, as
 231 extreme values can disproportionately influence the coefficient and distort the perceived
 232 relationship between predictions and observations. In contrast, RCOR measures the forecast
 233 system’s ability to correctly identify the relative ranking of years from least to most active in
 234 the observed record.

235 MSSS is defined by the following equation:

$$236 \quad MSSS \equiv 1 - \frac{\frac{1}{n} \sum_{i=1}^n (f_i^{obs} - f_i)^2}{\frac{1}{n} \sum_{i=1}^n (f_i^{obs} - f^{obs})^2}, \quad (1)$$

237 where n is the total number of years, f_i^{obs} and f_i are the values from observations and
 238 predicted values for the i^{th} year, respectively, and f^{obs} is the observational mean. The MSSS
 239 compares the model’s skill against climatological forecasts, with values greater than zero
 240 indicating better predictive skill than a climatological forecast (Kim et al., 2012; Li et al.,
 241 2013).

242 Throughout the analysis, unless presenting raw predicted results, both TC and large-
243 scale variables are normalized by subtracting the climatological mean and dividing by the
244 standard deviation, with these mean and standard deviation values specific to each model's
245 lead month. After normalization, RCOR and MSSS are computed. We assess the statistical
246 significance of RCOR using a two-tailed test, with the test statistic asymptotic t -distributed
247 with $n-2$ degrees of freedom, where n is the sample size, adjusted for observed autocorrelation
248 (Siegel and Castellan, 1988).

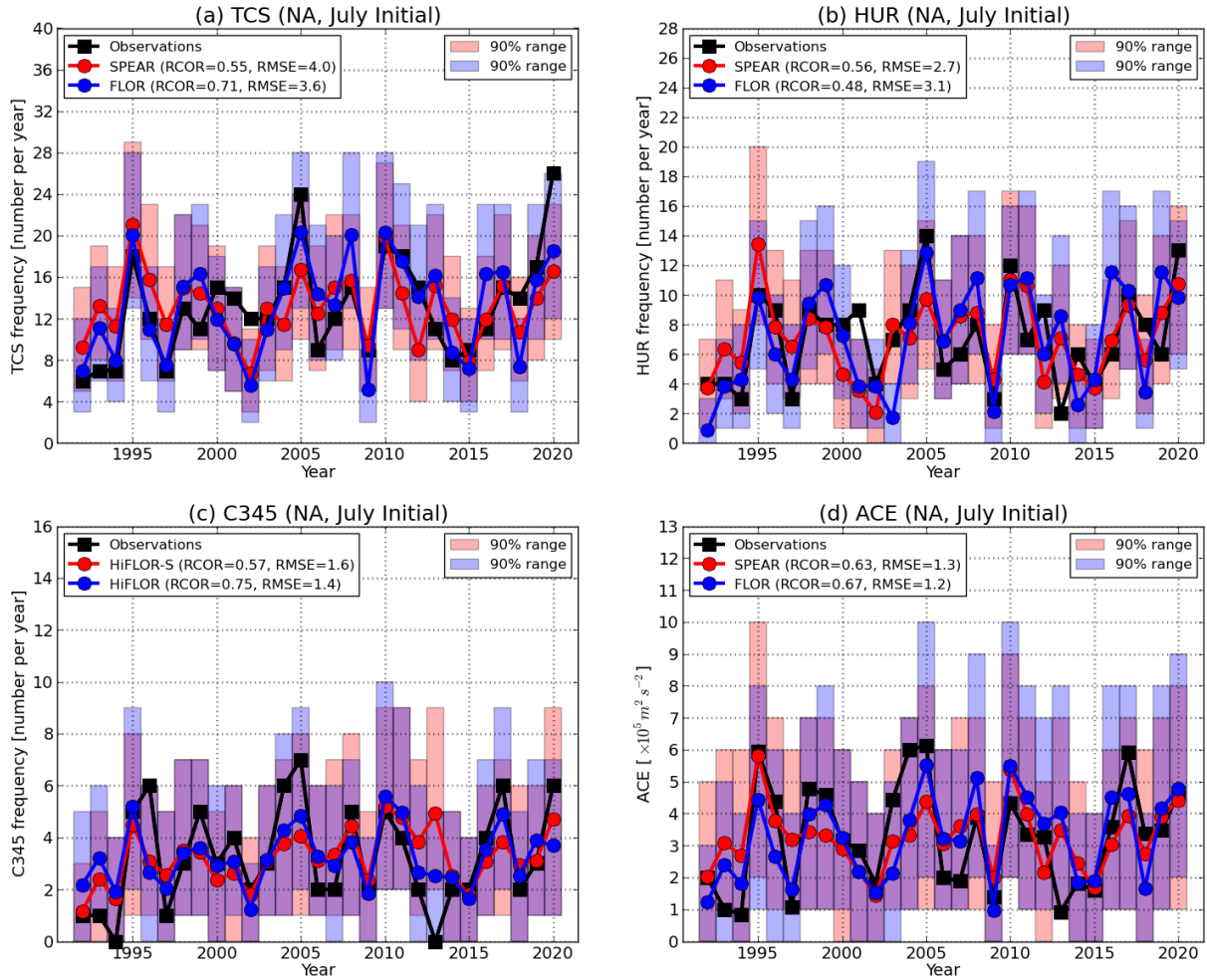
249 We also used the bootstrap method proposed by Murakami et al. (2013) to evaluate the
250 statistical significance of the mean difference between model experiments. Two tested
251 populations were resampled in pairs 2,000 times, and the mean difference for each pair was
252 calculated, creating a new distribution with 2,000 samples. A 95% confidence interval was
253 derived from this distribution and compared with the original mean difference.

254

255 **3. Results**

256 *a. Retrospective Forecast of Basin-Wide TC Activity*

257 We first compare the retrospective forecast skill in basin-wide seasonal TC activity
258 over the NA between FLOR and SPEAR and between HiFLOR and HiFLOR-S. Figure 1
259 shows the time series of observed and predicted TCS, HUR, C345, and ACE from the July
260 initial predictions (i.e., $L=0$). Generally, the new prediction system (i.e., SPEAR and HiFLOR-
261 S) exhibited similar though usually slightly lower skill than the previous prediction system
262 (i.e., FLOR and HiFLOR), although both systems show statistically significant correlations,
263 covering the observations within their 90% range estimated from the ensemble members.
264 There are some clear differences in active seasons between SPEAR and FLOR. For example,
265 SPEAR predicted a higher number of HUR for 1995 than FLOR (Fig. 1b). However, this
266 feature is inconsistent; for example, FLOR predicts a higher number of HUR for 2005 than
267 SPEAR.



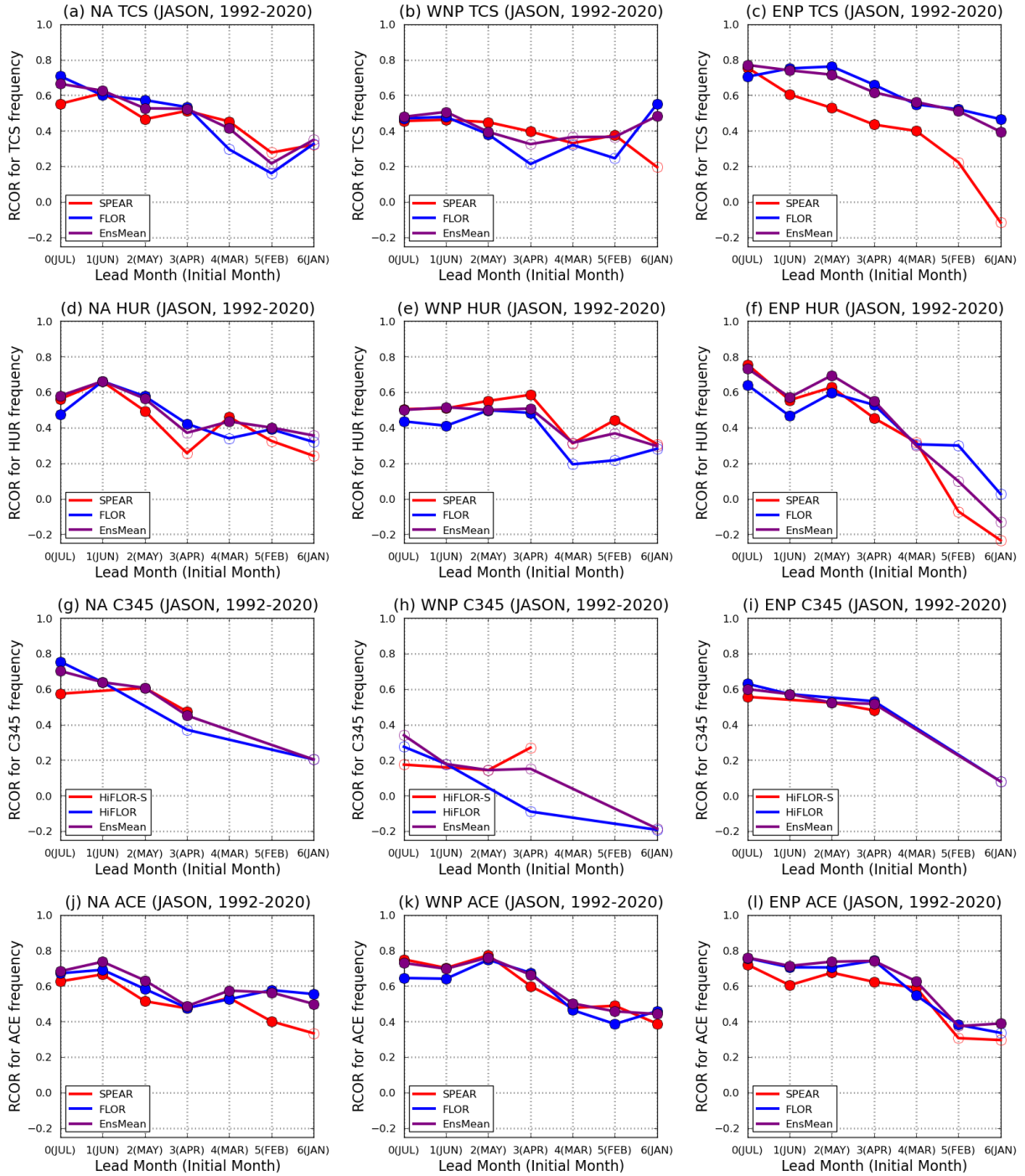
268

269 **FIG. 1** Retrospective predictions of (a) basin-wide frequency of TCS, (b) HUR, (c) C345, and
 270 (d) ACE in the NA during the peak TC season of July–November for the period 1992–2020
 271 initialized in July. The black lines represent the observed values, the red lines represent the
 272 mean values of the new prediction system (SPEAR or HiFLOR-S), and the blue lines
 273 represent the mean values of the previous prediction system (FLOR or HiFLOR). Shading
 274 indicates the 90% confidence intervals computed by convolving inter-ensemble spread based
 275 on the Poisson distribution. The values of “RCOR” and “RMSE” in each panel indicate the
 276 rank correlation coefficient and root-mean-square error between the predictions and
 277 observations, respectively. Units: number per year for TCS, HUR, and C345 and $10^5 \text{ m}^2 \text{ s}^{-2}$ per
 278 year for ACE.
 279

280 Figure 2 compares the RCOR skill of TC activities for each initial month. While Fig. 1
 281 indicates that the new prediction system worsens the prediction skill in the NA from the July
 282 initial conditions, this is not always the case for different initialization months. Overall, both
 283 SPEAR and FLOR demonstrate statistically significant skill in predicting TCS and HUR in the
 284 NA from lead-month 0 to 2 predictions (Figs. 2a,d). SPEAR also shows skillful predictions of

285 TCS and HUR at lead-month 4, although the skill at lead-month 3 is not statistically
286 significant. Additionally, Fig. 2 displays prediction skill for the WNP and ENP, revealing that
287 SPEAR generally outperforms (underperforms) FLOR for TCS and HUR predictions in the
288 WNP (ENP). For the comparison of C345 predictions between HiFLOR and HiFLOR-S, both
289 show comparable prediction skill across the three ocean basins (Figs. 2g–i). Generally, ACE
290 predictions exhibit skill even from February's initial predictions (Figs 2j,k,l), indicating greater
291 skill in ACE predictions compared with TC frequency predictions.

292 Previous studies have reported that ensemble means of multi-models often outperform
293 individual models in TC seasonal predictions (e.g., Vitart 2006; Vitart et al. 2007). In this
294 study, we also assessed the prediction skill of the ensemble means of SPEAR and FLOR
295 (shown by the purple lines in Fig. 2). Our findings indicate that the prediction skill of the
296 multi-model ensemble mean is not simply an average of the skill of the two individual models.
297 In some instances, the multi-model ensemble mean outperforms both models, particularly for
298 ACE predictions. This result highlights the potential for further improvements in prediction
299 skill by utilizing a multi-model ensemble approach.



300

301 **FIG. 2** RCORs between observed and predicted TC activity for each initial month from
 302 January (L6) to July (L0). (a)–(c) TCS, (d)–(f) HUR, (g)–(i) C345, and (j)–(l) ACE over (left)
 303 the NA, (middle) WNP, and (right) ENP. The red lines depict predictions by the new
 304 prediction system (SPEAR or HiFLOR-S), whereas the blue lines depict predictions by the
 305 previous prediction system (FLOR or HiFLOR). The purple lines are multi-model ensemble
 306 means of the new and previous prediction systems. Filled marks indicate statistically

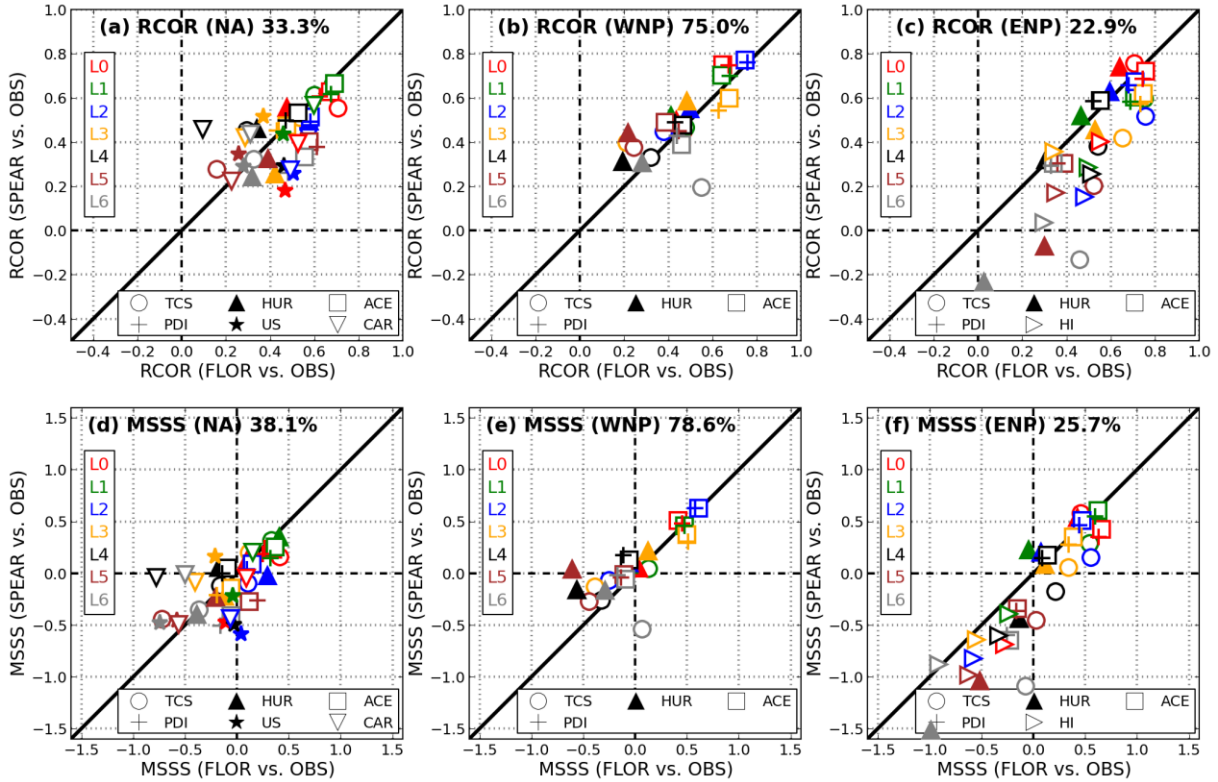
307 significant RCORs at a 95% confidence level, whereas open marks denote non-significant
308 RCORs.
309

310 To provide a more comprehensive quantification of how the TC metrics of the new
311 prediction system compare with those of the previous prediction system, we display scatter
312 plots of RCOR and MSSS in Fig. 3 for interannual variation of seasonal mean value between
313 observations and predictions. Here, we compare basin-wide frequencies of TCS, HUR,
314 landfalling frequencies of CAR and HI, and basin-total values of ACE and PDI. A marker
315 above the diagonal line indicates that SPEAR outperforms FLOR for the TC metric at the
316 specified lead month.

317 As expected, the shortest lead-month forecasts (e.g., L0 and L1) generally yield higher
318 RCOR and MSSS than the longer lead months (e.g., L5 and L6) for most of the TC variables.
319 It is also worth noting that models generally predict ACE better than TCS (Fig. 3), a finding
320 consistent with previous studies (e.g., Murakami et al., 2016a). Overall, SPEAR outperforms
321 FLOR for the TC predictions over the WNP (75–79%), whereas SPEAR underperforms FLOR
322 over the NA (33–38%) and ENP (23–26%) where the parentheses indicate the fraction of the
323 number of variables that SPEAR outperforms FLOR relative to the total number of the
324 variables.

325 Similar trends are obtained for the comparisons between HiFLOR-S and HiFLOR
326 (Supplementary Fig. 1). Generally, HiFLOR-S outperforms HiFLOR for the NA (60–62%),
327 WNP (64–71%), but underperforms HiFLOR or comparable for the ENP (49%), where the
328 parentheses indicate the fraction of the number of variables that HiFLOR-S outperforms
329 HiFLOR.

330



331

332 **FIG. 3** Scatterplots of RCOR between SPEAR prediction and observations (y -axis) and FLOR
 333 prediction and observations (x -axis) for the (a) NA, (b) WNP, and (c) ENP. (d–f) As in (a–c),
 334 but for MSSS. A marker positioned above the diagonal line indicates that SPEAR exhibits
 335 higher skill than FLOR. The variables evaluated include basin-wide frequency of TCS, HUR,
 336 basin-wide values of ACE, PDI, and the landfalling TC frequency for the Continental United
 337 States (US), Caribbean Islands (CAR), and Hawaiian Islands (HI). Different colors represent
 338 different lead months (L0–L6). Percentages on the plots denote the fraction of variables in
 339 which SPEAR outperforms FLOR relative to the total number of variables evaluated.

340

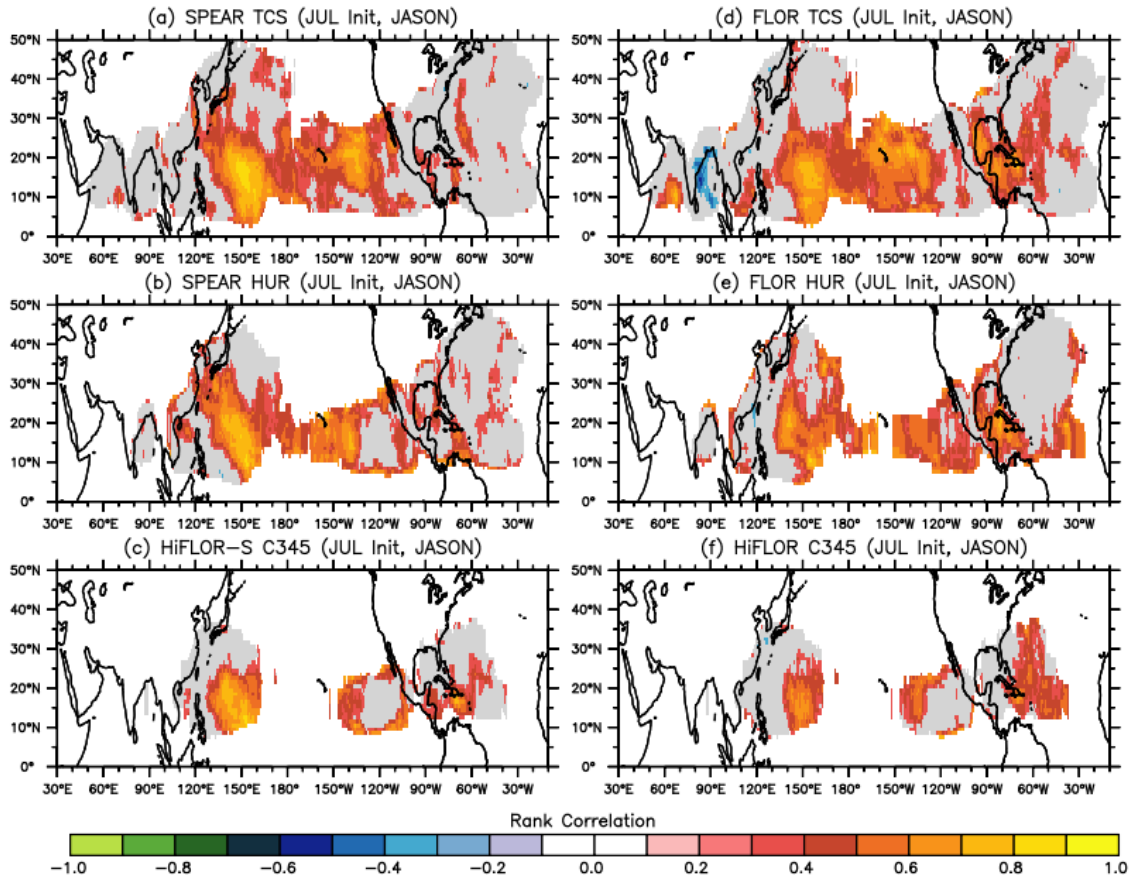
341 *b. Retrospective Predictions of Landfalling and Regional TC Activity*

342 Beyond the prediction skill of basin-wide TC variables, we evaluate prediction skill in
 343 regional TC activity in terms of landfall TCs (i.e., US, CAR, and HI) and the frequency of TC
 344 occurrence.

345 Supplementary Figs. 2 and 3 show results similar to Figs. 2 and 3, focusing exclusively
 346 on landfalling predictions (i.e., US, CAR, and HI). Regarding RCOR, SPEAR exhibits lower
 347 prediction skill for HI compared to FLOR across most lead-month predictions. For US and
 348 CAR, results are mixed: SPEAR outperforms FLOR in a few lead-month predictions (e.g., L3
 349 or L4). In terms of MSSS, no clear differences are observed between SPEAR and FLOR.

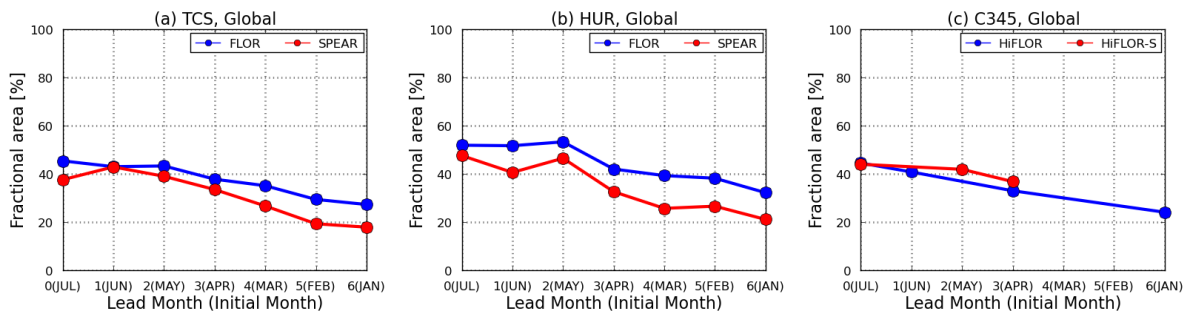
350 Figure 4 displays the prediction skill as measured by RCOR between L0 predictions by
351 the models and observations for each grid cell. Both SPEAR and FLOR demonstrate
352 statistically significant skill in the central Pacific for TCS, particularly around Hawaii,
353 indicating their ability to predict the frequency of landfalling TCs over the Hawaiian Islands.
354 SPEAR also exhibits improved prediction skill for TCS and HUR near Japan relative to FLOR
355 (Figs. 4a,b,d,e). In contrast, SPEAR shows degraded prediction skill for landfalling storms
356 over the NA relative to FLOR. HiFLOR-S shows comparable skill to HiFLOR in terms of
357 C345 in the Pacific Ocean, but HiFLOR-S demonstrates degraded prediction skill over the NA
358 (Figs. 4c, f).

359 We counted the number of grids where the model shows statistically significant
360 positive RCOR with observations (i.e., red and yellow shadings in Fig. 4). This number was
361 then divided by the total number of valid grid cells where the observed frequency of
362 occurrence is nonzero for at least 25% of years (i.e., seven years; all grids within the gray
363 shading in Fig. 4). This fractional number is compared between the models on a global scale
364 for each TC category and lead month (Fig. 5). Figure 5 indicates that SPEAR generally
365 demonstrates a smaller area of skillful predictions for TCS and HUR relative to FLOR,
366 although differences between HiFLOR-S and HiFLOR for C345 are marginal. Overall, we did
367 not find clear improvements in prediction skill for TC activity at the regional scale with the
368 new prediction system compared to the previous prediction system.



369

370 **FIG. 4** Skill of frequency of occurrence of TCs during July–November 1992–2020 for the
 371 retrospective forecasts initialized in July. Shading indicates the retrospective RCOR of
 372 predicted versus observed TC frequency of occurrence ($1^\circ \times 1^\circ$ grid box), masked at a two-
 373 sided $p=0.1$ level. Results are shown for (a) TCS for SPEAR, (b) HUR for SPEAR, and (c)
 374 C345 for HiFLOR-S. (d–f) As in (a–c), bur for FLOR and HiFLOR. Gray shading in all panels
 375 indicates that observed TC density is nonzero for at least 25% of years (i.e., seven years).
 376



377

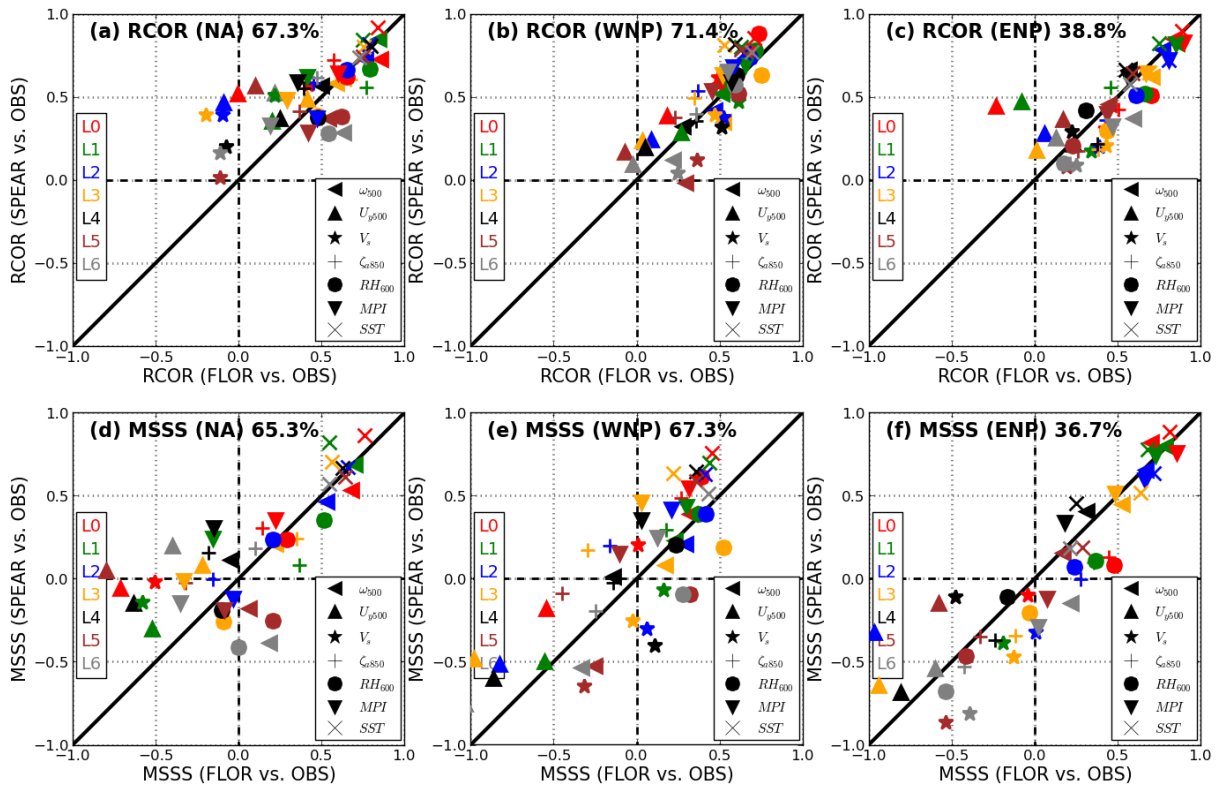
378 **FIG. 5** Fractional number of grids with statistically significant positive RCOR between
 379 predictions and observations relative to the total number of valid grids on a global scale. Valid
 380 grids are defined as grids where the observed TC density is nonzero for at least 25% of the

381 years (i.e., seven years; gray areas in Fig. 4). Shown for (a) TCS for SPEAR and FLOR, (b)
 382 HUR for SPEAR and FLOR, and (c) C345 for HiFLOR-S and HiFLOR.
 383

384 *c. Retrospective Predictions of Large-scale Variables*

385 Previous studies have suggested that improving the simulation of large-scale variables
 386 could result in improved simulations of TC activity (Vecchi et al., 2014; Murakami et al.,
 387 2015; Krishnamurthy et al., 2016). It is expected that improving prediction skill in large-scale
 388 variables should be linked to improving prediction skill in TC variables. However, this is not
 389 always the case. For example, Murakami et al. (2016a) revealed that the changes in prediction
 390 skill in large-scale variables are not always relevant to the changes in prediction skill in TC
 391 activity in the NA. To examine whether the differences in prediction skill in TC variables
 392 between the new and previous prediction systems, as shown in Section 3a,b are linked to the
 393 changes in prediction skill in large-scale variables, we compare the prediction skill in the TC-
 394 relevant large-scale variables.

395 Figure 6 compares the RCOR and MSSS between the observed and predicted large-
 396 scale variables in the key main development region for each basin by FLOR (*x*-axis) and
 397 between observed and predicted by SPEAR (*y*-axis).



398

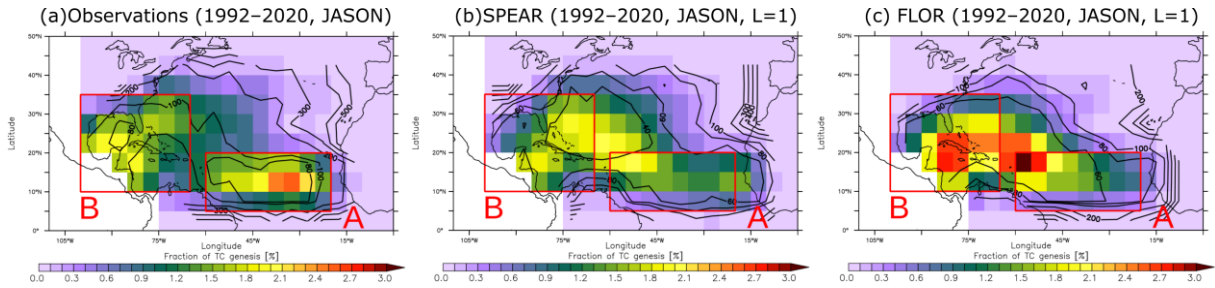
399 **FIG. 6** As in Fig. 3, but for large-scale variables over the main development regions. Variables
400 evaluated (symbols in the bottom right) are ω_{500} , U_{y500} , V_s , ζ_{a850} , RH_{600} , MPI , and SST .
401

402 For the NA, more than half of the variables are located above the diagonal lines,
403 indicating improved skill in the large-scale variables in SPEAR over FLOR (Figs. 6a and d),
404 although SPEAR showed lower skill in TC metrics than FLOR (Figs. 3a and d). These results
405 are consistent with those of Murakami et al. (2016a), who reported that the improvements in
406 predicting TC activity over the NA are not directly related to the improvements in predicting
407 large-scale variables. In contrast, the WNP and ENP are relatively consistent between large-
408 scale variables and TC activity compared to the NA (Fig. 3 and Fig. 6). For the comparisons
409 between HiFLOR-S and HiFLOR, differences in prediction skill for large-scale variables
410 correspond well with differences in TC variables for RCOR (Supplementary Figs. 1 and 4).

411 Here, we aim to identify the reasons for the discrepancies in prediction skill between
412 TC-related variables and large-scale variables when comparing SPEAR and FLOR in the NA.
413 Differences in TC prediction skill between these models may stem from differences in the
414 simulations of TC climatology and/or differences in how TC climatology responds to large-
415 scale conditions. To start, we compared the spatial distributions of the climatological mean TC
416 genesis frequency between observations and models, SPEAR and FLOR, in the NA (shadings
417 in Fig. 7 and Table 2).

418 This comparison reveals that differences in the predicted climatological mean TC
419 genesis frequency between the models do not fully explain why FLOR exhibits better NA TC
420 prediction skill than SPEAR. For example, observations show frequent TC genesis in both the
421 eastern tropical Atlantic (Domain A) and the western tropical Atlantic (Domain B), with
422 slightly higher TC genesis frequency in Domain B than in Domain A (Fig 7a and Table 2).
423 However, both SPEAR and FLOR display notable biases in the mean locations of TC genesis
424 (Figs. 7b, c), underestimating TC genesis frequency in Domain A and showing increased
425 frequency in the central tropical Atlantic compared to observations.

426



427

428 **FIG. 7** Climatological mean TC genesis frequency and the standard deviation of interannual
 429 variability during July–November for the period 1992–2020. (a) Observations, (b) lead-month
 430 1 predictions by SPEAR, and (c) lead-month 1 predictions by FLOR. Shadings represent the
 431 fraction of the climatological mean TC genesis frequency at each grid cell relative to the ocean
 432 basin total [Units: %]. Contours indicate the standard deviation of interannual variability,
 433 normalized by the climatological mean TC genesis frequency at each grid cell [Units: %]. Red
 434 rectangles highlight the main development regions, A and B.
 435

436 **Table 2** Climatological mean TC genesis frequency and the amplitude of interannual variation
 437 of TC genesis frequency for Domains A and B. Displayed are the fraction of climatological
 438 mean TC genesis frequency (total TC genesis frequency within a domain divided by the basin-
 439 total TC genesis frequency [%]) and the fraction of standard deviation relative to the
 440 climatological mean TC genesis frequency (standard deviation of interannual variation of total
 441 TC genesis frequency within a domain divided by the climatological mean TC genesis
 442 frequency for the same domain [%]).
 443

	Fraction of climatological mean TC genesis frequency over a domain relative to the basin-total TC genesis frequency [%]		Fraction of standard deviation of interannual variation of TC genesis frequency relative to the climatological mean TC genesis frequency [%]	
	Domain A	Domain B	Domain A	Domain B
Observations	34.2%	38.6%	81.3%	104.7%
SPEAR	26.4%	35.4%	58.5%	50.6%
FLOR	28.4%	42.8%	59.3%	60.4%

444

445 On the other hand, substantial differences exist in the amplitude of interannual
 446 variation in TC genesis frequency between the models, which may further contribute to
 447 differences in TC prediction skill. For instance, observations show marked interannual
 448 variation in both Domains A and B, with the standard deviation exceeding 80% of the
 449 climatological mean TC genesis frequency (contours in Fig. 7 and Table 2). Although both

450 FLOR and SPEAR underestimate the amplitude of interannual variations in both domains,
 451 FLOR’s amplitude is closer to observed values than SPEAR’s, particularly in Domain B.

452 Furthermore, FLOR simulates a more accurate sensitivity of TC genesis frequency to
 453 large-scale variables in both Domains A and B than SPEAR (Table 3). For example,
 454 observations indicate that TC genesis frequency in Domain A is more highly correlated with
 455 thermodynamical variables (e.g., RH_{600} and SST) than with dynamical variables (e.g., V_s and
 456 ζ_{a850}). Conversely, in Domain B, it is more highly correlated with dynamical variables than
 457 thermodynamical ones. Although the RCORS produced by both models differ notably from
 458 observations, FLOR captures these observed tendencies better than SPEAR.

459

460 **Table 3** RCORs of interannual variations between the TC genesis frequency and large-scale
 461 variables for each domain (1992–2020). The numbers in bold and underscore highlight the two
 462 highest correlations among the variables for each observation and model.

463

	V_s	ζ_{a850}	RH_{600}	MPI	SST
Domain A					
Observations	-0.24	+0.39	<u>+0.56</u>	+0.35	<u>+0.42</u>
SPEAR	<u>-0.60</u>	+0.52	+0.57	<u>+0.82</u>	+0.35
FLOR	-0.25	+0.33	<u>+0.81</u>	<u>+0.83</u>	+0.79
Domain B					
Observations	<u>-0.43</u>	<u>+0.54</u>	-0.11	-0.22	+0.00
SPEAR	-0.54	<u>+0.89</u>	<u>+0.78</u>	-0.31	+0.09
FLOR	<u>-0.64</u>	<u>+0.90</u>	-0.43	-0.32	+0.12

464

465 Previous studies suggest that ENSO, Madden Julian Oscillation (MJO), and tropical
 466 upper-tropospheric troughs (TUTT) associated with extratropical Rossby wave breaking
 467 influence wind shear and low-level vorticity in Domain A, while the Atlantic Meridional Mode
 468 (AMM) affects SST and relative humidity in Domain B (e.g., Maloney and Hartmann 2000;
 469 Kossin and Vimont 2007; Wang et al. 2020). Differences in teleconnection patterns or the
 470 influence of interannual climate modes on atmospheric conditions between the models may
 471 contribute to the variations in TC seasonal prediction skill in the NA.

472 With its higher horizontal resolution, HiFLOR-S is expected to outperform SPEAR in
 473 predicting TC variables, especially in intense storms such as C345. However, since the
 474 HiFLOR-S predictions were forced with SSTs predicted by SPEAR, differences in TC

475 predictions between SPEAR and HiFLOR-S likely result from differences in the response of
476 model-simulated TCs or large-scale variables to the same SSTs. Supplementary Figs. 5 and 6
477 display the same plots as Figs. 3 and 6, respectively, but for the comparisons between
478 HiFLOR-S and SPEAR. Generally, the prediction skill differences between SPEAR and
479 HiFLOR-S for TC variables do not align with those for large-scale variables except in the
480 WNP. For example, the prediction skill of large-scale variables is lower (higher) in HiFLOR-S
481 than in SPEAR in the NA (ENP). However, these skill differences in large-scale variables do
482 not correspond to those of TC variables (Supplementary Fig. 5); HiFLOR-S generally
483 outperforms (underperforms) SPEAR for TC variables in the NA (ENP). This finding
484 reinforces the notion that higher prediction skill in large-scale variables do not necessarily lead
485 to higher prediction skill in TC variables.

486 We compared the spatial pattern of the climatological mean TC genesis frequency and
487 interannual variations between SPEAR and HiFLOR-S for L3 predictions, where HiFLOR-S
488 outperforms better than SPEAR in TC predictions for the NA. Supplementary Fig. 7 indicates
489 that HiFLOR-S has a less accurate spatial pattern of climatological TC genesis frequency than
490 SPEAR. Specifically, TC genesis frequency in HiFLOR-S is heavily concentrated around the
491 central tropical Atlantic, with a higher genesis frequency in Domain A than in Domain B
492 (Supplementary Table 1). This again suggests that differences in climatological TC genesis
493 frequency alone do not fully explain the variations in TC prediction skill. Meanwhile, the
494 amplitude of interannual variation in TC genesis frequency in Domain B is larger and more
495 aligned with observations in HiFLOR-S compared to SPEAR (Supplementary Table 1).
496 Additionally, the RCORs of interannual variations between TC genesis frequency and large-
497 scale variables are more accurate in HiFLOR-S than SPEAR for both Domains A and B
498 (Supplementary Table 2).

499 Overall, these results emphasize that differences in TC predictions between models
500 likely stem from biases in the models' sensitivity of TCs to large-scale variables, as well as
501 biases in the amplitude of interannual variation in TC genesis frequency across the main
502 development regions. This underscores that even when a model accurately predicts large-scale
503 variables, its TC predictions could still be inaccurate.

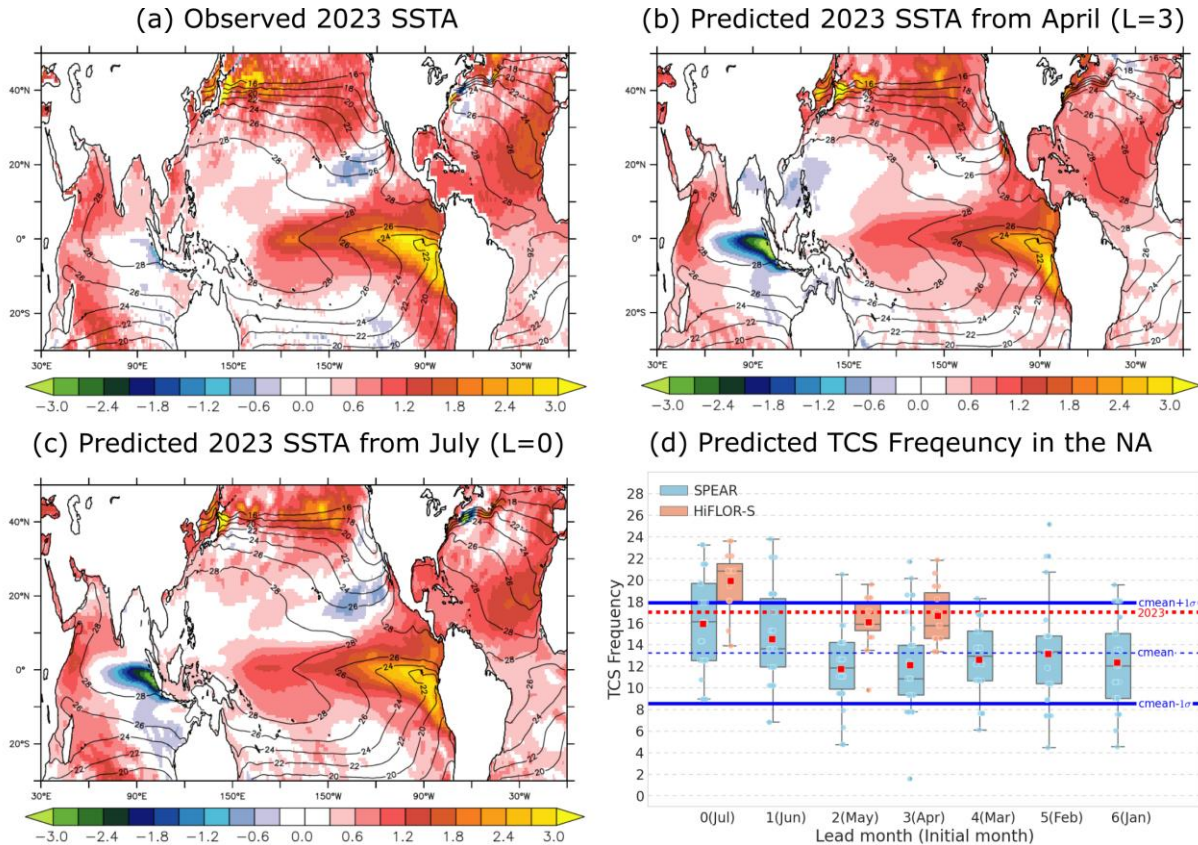
504

505 *d. Difference in 2023 summer predictions between SPEAR and HiFLOR-S*

506 When we conducted real-time seasonal predictions for the summer of 2023, a notable
507 discrepancy between SPEAR and HiFLOR-S in the TC predictions became apparent. The
508 2023 summer season was characterized by a strong El Niño development and warmer-than-
509 average tropical North Atlantic (Fig. 8a). It is empirically known that, during El Niño
510 developing summers, TCs are less active than normal over the NA due to strong vertical shears
511 (e.g., Goldenberg et al., 1996; Smith et al., 2010). In contrast, previous studies have revealed
512 that warmer tropical Atlantic conditions could lead to active TC seasons in the NA (e.g.,
513 Vecchi et al., 2011; Villarini et al., 2010; Murakami et al., 2018). Therefore, these
514 contradicting SST conditions could result in either an active or inactive TC season in the NA.

515 As revealed in Figs. 8b,c, SPEAR accurately predicted the observed SST anomaly,
516 even from the April 2023 initial predictions. Figure 8d highlights marked differences in the
517 TCS predictions between SPEAR and HiFLOR-S. Until the May initial predictions, SPEAR
518 predicted, in the ensemble mean, approximately 12 TCSs, whereas HiFLOR-S predicted
519 around 17 TCSs. The observed TCS count was 17 in 2023, indicating that the HiFLOR-S
520 predictions were more accurate than the SPEAR predictions. SPEAR adjusted its predictions
521 to reflect a more active TC season from the June and July initial predictions compared to the
522 previous month's predictions (Fig. 8d).

523

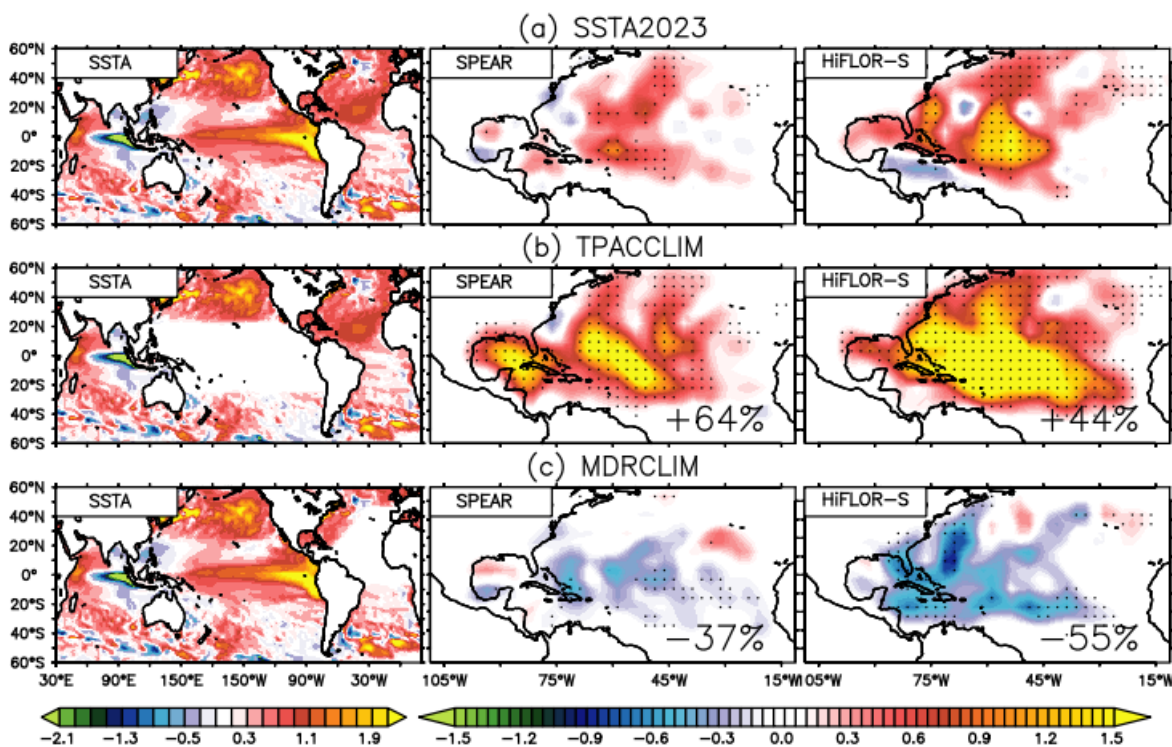


524

525 **FIG. 8** Observed and predicted SST anomaly and TCS frequency over the NA during July–
 526 November 2023. (a) Observed 2023 SST anomaly, predicted 2023 SST anomaly from (b)
 527 April and (c) July initial conditions by SPEAR, and (d) Observed and predicted TCS
 528 frequency over the NA for each lead month prediction by SPEAR and HiFLOR-S. Shadings
 529 and contours in (a)–(c) represent SST anomalies and climatological mean SSTs, respectively.
 530 The dashed red line in (d) represents the 2023 observed TCS frequency, while the dashed blue
 531 line represents the observed climatological mean TCS frequency. Blue solid lines in (d)
 532 indicate the range of $\pm 1\sigma$ of the observed interannual variation. The red squares in (d)
 533 represent the ensemble mean values, whereas the dots represent values for each ensemble
 534 member. The boxes in (d) represent the lower and upper quartiles, with the horizontal lines
 535 showing the median value and the end lines showing the lowest datum still within the 1.5
 536 interquartile range (IQR) of the lower quartile and the highest datum still within the 1.5 IQR
 537 of the upper quartile.
 538

539 To assess the relative influence of the 2023 El Niño and warmer Atlantic SSTs on TCS
 540 frequency in the NA, we conducted idealized real-time attribution experiments using SPEAR
 541 and HiFLOR-S (Murakami et al., 2017, 2018; Qian et al., 2019; Nasuno et al., 2022). Similar
 542 to the HiFLOR-S predictions, we performed predictions using SPEAR and HiFLOR-S, which
 543 were forced with the predicted SSTs derived from the real-time 2023 April initial predictions
 544 by SPEAR but with some modifications. We conducted 15-member ensemble experiments

545 from the 15-member SSTs predicted by SPEAR. Specifically, we replaced the SSTs over the
 546 tropical Pacific with climatological mean values to eliminate the 2023 El Niño conditions,
 547 denoted as the TPACCLIM experiment (Fig. 9b). Similarly, we removed the anomalously
 548 warm tropical Atlantic conditions, referred to as the MDRCLIM experiment (Fig. 9c). These
 549 experiments were compared with those using the original 2023 predicted SSTs, termed the
 550 SSTA2023 experiment (Fig. 9a), and the climatological man SSTs, termed the CLIM
 551 experiment.

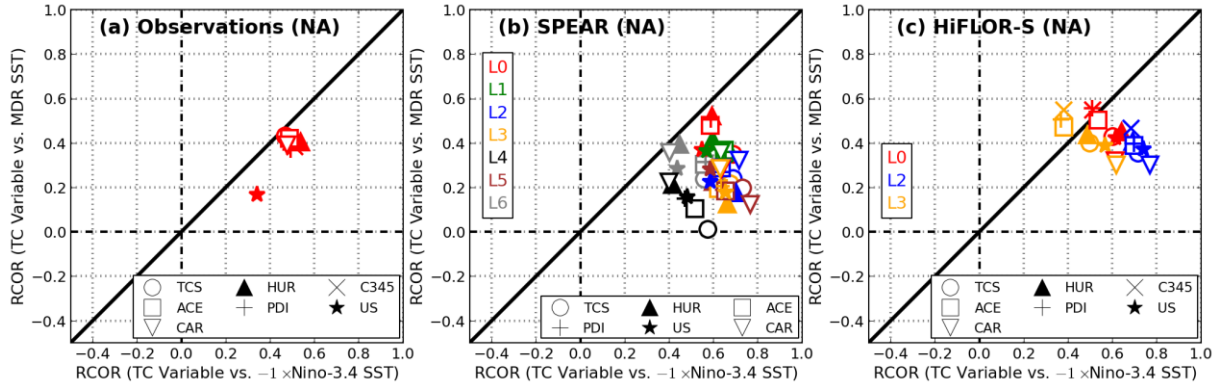


552

553 **FIG. 9** Prescribed idealized SST anomaly (SSTA) and simulated anomaly of TC frequency of
 554 occurrence. Idealized seasonal predictions are conducted by prescribing the idealized SSTs in
 555 which SSTAs (left panels; units: K) are superimposed onto the climatological mean SST
 556 (CLIM). The resultant predicted TC frequency of occurrence anomalies relative to the CLIM
 557 experiment are shown by the shading in the middle- and right-hand panels (units: number per
 558 season every $5^{\circ} \times 5^{\circ}$ grid cell). The prescribed SSTAs are (a) all 2023 anomalies (SSTA2023);
 559 (b) as in SSTA2023, except the tropical Pacific SSTAs are set to zero (TPACCLIM); (c) as in
 560 SSTA2023, except the tropical Atlantic SSTAs are set to zero (MDRCLIM). Dots in the
 561 middle- and right-hand panels indicate the predicted change relative to the CLIM experiment
 562 is statistically significant at the 95% confidence level or above by a bootstrap method. The
 563 numbers in (b) and (c) denote fractional changes in TCS frequency relative to the SSTA2023
 564 experiments.
 565

566 Because El Niño conditions are expected to suppress TC activity in the NA, removing
567 the 2023 El Niño through the TPACCLIM experiments is expected to result in more TCS
568 frequency in the NA than in the SSTA2023 experiments. Likewise, removing the tropical
569 Atlantic SST anomaly through the MDRCLIM experiments is expected to result in lower TCS
570 frequency than in the SSTA2023 experiments. As expected, TCS frequency increases by about
571 64% in the SPEAR TPACCLIM experiments relative to the SSTA2023 experiments (Fig. 9b).
572 In contrast, TCS frequency decreases by about 37% in the SPEAR MDRCLIM experiments
573 (Fig. 9c). These magnitudes of the changes indicate that SPEAR is more sensitive to the El
574 Niño condition than the tropical Atlantic SST for the TC activity in the NA. Meanwhile, TCS
575 frequency increases by about 44% in the HiFLOR-S TPACCLIM experiments (Fig. 9b).
576 However, the magnitude of the change is less than in the MDRCLIM experiments, in which
577 TCS frequency was decreased by 55% (Fig. 9c). Therefore, in contrast to SPEAR, HiFLOR-S
578 is more sensitive to the tropical Atlantic SST than the El Niño condition for TC activity in the
579 NA.

580 Figure 10 illustrates the RCORs between Niño-3.4 SST and TC metrics in the NA
581 compared with the RCORs between MDR SST and TC metrics for the observations and the
582 retrospective seasonal predictions by SPEAR and HiFLOR-S during 1992–2020. Observations
583 reveal that RCORs for most TC metrics other than US are around +0.4 with MDR SST and
584 +0.5 with Niño-3.4 SST with a flipped sign (Fig. 10a). The April initial predictions by SPEAR
585 (orange marks in Fig. 10b) reveal RCORs around +0.2 with MDR SST and +0.65 with Niño-
586 3.4 SST with a flipped sign, indicating SPEAR is more sensitive to Niño-3.4 SST than MDR
587 SST for NA TC variables compared to the observations. In contrast, those by HiFLOR-S
588 (orange marks in Fig. 10c) show RCORs around +0.4 with MDR SST and +0.5 with Niño-3.4
589 with a flipped sign, closer to the observations than SPEAR. It is noted that shorter lead month
590 predictions from SPEAR (e.g., red marks of L0) are relatively closer to the observations and
591 HiFLOR-S than the longer lead month predictions (e.g., black marks of L4). These results are
592 consistent with the 2023 summer predictions (blue plots in Fig. 8d), in which SPEAR changed
593 to predict a more active season in the shorter lead month predictions than the longer lead
594 month predictions. These results highlight that even given the same SST conditions, models
595 would respond differently to the SST, resulting in different TC predictions.



596

597 **FIG. 10** Scatterplots of RCORs between TC variables and MDR SST (y-axis) and TC
 598 variables and Niño-3.4 SST with the reversed sign (x-axis) for the NA TC activity. (a)
 599 Observations from 1992–2020. Markers above the diagonal lines indicate a stronger
 600 relationship with the MDR SST compared with the Niño-3.4 SST. (b) Retrospective seasonal
 601 predictions by SPEAR and (c) HiFLOR-S during 1992–2020. Different colors indicate
 602 different lead month predictions (L0–L6). Evaluated TC variables are the same as those in Fig.
 603 3.
 604

605 4. Summary

606 In this study, we evaluated the skill of retrospective seasonal predictions of TC activity
 607 using the new seasonal prediction system (SPEAR and HiFLOR-S) compared to the previous
 608 seasonal prediction system (FLOR and HiFLOR) developed at GFDL. Our analysis focused
 609 on predicting various aspects of TC activity, including basin-wide frequency of different
 610 categories of TC intensity, ACE, PDI, and landfalling TCs. Additionally, we examined relevant
 611 large-scale variables from July–November across the NA, WNP, and ENP ocean basins.

612 SPEAR consistently demonstrates skillful predictions of TC activity across the three
 613 ocean basins. Regarding basin-wide TC frequency, SPEAR exhibits statistically significant
 614 rank correlation skill up to lead month 4 (i.e., March initial conditions), with rank correlation
 615 coefficients ranging from +0.4 to +0.6 for the NA, +0.4 to +0.5 for the WNP, and +0.4 to +0.8
 616 for the ENP. However, when compared to FLOR, SPEAR yields comparable or lower skill in
 617 TC activity for the NA and ENP but exhibits higher skill for the WNP. Similarly, like
 618 HiFLOR, HiFLOR-S demonstrates statistically significant rank correlation skill in predicting
 619 major hurricanes in the NA, even from April's initial predictions, with rank correlation
 620 coefficients ranging from +0.4 to +0.6. HiFLOR-S generally exhibits higher skill in TC
 621 activity for the NA and WNP but demonstrates comparable skill in the ENP compared to

622 HiFLOR. Our analysis also indicates that the multi-model ensemble mean can sometimes
623 outperform individual model predictions, underscoring the potential for enhancing prediction
624 skill by integrating multiple models.

625 We further examined the prediction skill of regional TC activity in terms of TC
626 frequency of occurrence and landfalling storms. SPEAR generally underperforms FLOR in
627 landfall predictions in the coastal areas of the U.S., Caribbean islands, and Hawaii. While
628 SPEAR exhibited smaller areas of skillful predictions of regional TC activity compared to
629 FLOR, SPEAR exhibited skillful predictions of regional TC activity near Japan. This suggests
630 skillful landfalling TC predictions in the region.

631 We assessed prediction skill in TC-relevant large-scale variables to determine whether
632 the different prediction skill in TC variables between the previous and new prediction systems
633 could be attributed to differences in prediction skill in large-scale variables. However, this
634 analysis revealed that the two do not always correspond, particularly for the NA, which aligns
635 with findings from previous studies (e.g., Murakami et al., 2016a). Further analysis indicated
636 that the amplitude of interannual variations in TC genesis frequency plays a crucial role in
637 prediction skill. Moreover, the sensitivity of TCs to large-scale parameters varies by region.
638 For instance, TC genesis frequency over the eastern tropical NA is more sensitive to
639 thermodynamical variables than to dynamical variables, while the opposite is true for the
640 western tropical NA. Accurately simulating these sensitivities is key to improving TC
641 prediction.

642 Through idealized and retrospective seasonal predictions, SPEAR demonstrates greater
643 sensitivity to El Niño conditions, while HiFLOR-S shows less sensitivity to El Niño compared
644 to warmer SSTs in the MDR for predicting NA TC variables. This sensitivity discrepancy
645 resulted in conflicting TC predictions for the 2023 summer season when both El Niño
646 conditions and warmer MDR SSTs in the NA were predicted simultaneously. This underscores
647 the importance of not only improving the prediction skill of SSTs themselves but also
648 enhancing the model's response of TCs to such large-scale conditions like SSTs to achieve
649 further improvement in TC prediction skill at a seasonal time scale.

650

651 *Acknowledgments*

652 The statements, findings, and conclusions are those of the authors and do not necessarily
653 reflect the views of the National Oceanic and Atmospheric Administration, the U.S.
654 Department of Commerce, or the U.S. Army Corps of Engineers. We thank Drs. Jaeyeon Lee
655 and Jan-Huey Chen for their valuable comments and suggestions. The authors declare no
656 competing financial interests. Correspondence and requests for materials should be addressed
657 to Hiroyuki Murakami.

658

659 *Data Availability*

660 The observed TC data (IBTrACS) are publicly available at
661 <https://www.ncdc.noaa.gov/ibtracs/>. The observed SST data (OISST) are available at
662 <https://www.ncei.noaa.gov/products/optimum-interpolation-sst>. The JRA-55 reanalysis
663 datasets are available at https://jra.kishou.go.jp/JRA-55/index_en.html. The model outputs by
664 SPEAR are available through the NMME webpage:
665 <https://www.cpc.ncep.noaa.gov/products/NMME/data.html>. The datasets analyzed during the
666 current study are available at <https://doi.org/XXX> (The data will be uploaded upon the
667 acceptance of this manuscript). These uploaded files are freely available.

668

669 **References**

- 670 Adcroft, A., and Coauthors, 2019: The GFDL global ocean and sea ice model OM4.0: Model
671 description and simulation features. *J. Adv. Model. Earth Syst.*, **11**, 3167–3211,
672 doi:10.1029/2019MS0017268.
- 673 Befort, D. J., K. I. Hodges, and A. Weisheimer, 2022: Seasonal Prediction of Tropical
674 Cyclones over the North Atlantic and Western North Pacific. *J. Climate*, **35**, 1385–1397,
675 doi:10.1175/JCLI-D-21-0041.1.
- 676 Bell, G. D. *et al.*, 2000: The 1999 North Atlantic and Eastern North Pacific hurricane season
677 [in “Climate Assessment for 1999”]. *Bull. Amer. Meteor. Soc.*, **81** (6), S19–S22,
678 doi:10.1175/15200477(2000)081<1328:CAF>2.3.CO;2.
- 679 Bister, M., and K. A. Emanuel, 1998: Dissipative heating and hurricane intensity. *Meteor.*
680 *Atmos. Phys.*, **52**, 233–240, doi:10.1007/BF01030791.
- 681 Bushuk, M., M. Winton, A. F. Haumann, T. Delworth, F. Lu, Y. Zhang, L. Jia, L. Zhang, W.
682 Cooke, M. Harrison, B. Hurlin, N. C. Johnson, S. Kapnick, C. McHugh, H. Murakami, A.
683 Rosati, K. Tseng, A. T. Wittenberg, X. Yang, and F. Zeng, 2021: Seasonal prediction and
684 predictability of regional Antarctic sea ice. *J. Climate*, **34**, 6207–6233, doi:10.1175/JCLI-
685 D-20-0965.1.
- 686 Bushuk, M., Y. Zhang, M. Winton, B. Hurlin, T. Delworth, F. Lu, L. Jia, L. Zhang, W. Cooke,
687 M. Harrison, N. C. Johnson, S. Kapnick, C. McHugh, H. Murakami, A. Rosati, K. Tseng,
688 A. T. Wittenberg, X. Yang, and F. Zeng, 2022: Mechanisms of regional Arctic sea ice
689 predictability in two dynamical seasonal forecast systems. *J. Climate*, **35**, 4207–4231,
690 doi:10.1175/JCLI-D-21-0544.1.
- 691 Camargo, S. J., A. G. Barnston, P. J. Klotzbach, and C. W. Landsea, 2007: Seasonal tropical
692 cyclone forecasts. *WMO Bull.*, **56**, 297–309.
- 693 Camp, J., M. Roberts, C. MacLachlan, E. Wallace, L. Hermanson, A. Brookshaw, A. Arribas,
694 and A.A. Scaife, 2015: Seasonal forecasting of tropical storms using the Met Office
695 GloSea5 seasonal forecast system. *Quart. J. Roy. Meteor. Soc.*, **141**, 1975–2470,
696 doi:10.1002/qj.2516.
- 697 Chang, Y. -S., S. Zhang, A. Rosati, T. L. Delworth, and W. F. Stern, 2013: An assessment of
698 oceanic variability for 1960–2010 from the GFDL ensemble coupled data
699 assimilation. *Clim. Dyn.*, doi:10.1007/s00382-012-1412-2.

700 Chen, J.-H. and S.-J. Lin, 2011: The remarkable predictability of inter-annual variability of
701 Atlantic hurricanes during the past decade. *Geophys. Res. Lett.*, **38**, L11804,
702 doi:10.1029/2011GL047629.

703 Chen, J.-H. and S.-J. Lin, 2013: Seasonal predictions of tropical cyclones using a 25-km-
704 resolution general circulation model. *J. Climate*, **26**, 380–398, doi:10.1175/JCLI-D-12-
705 00061.1

706 Chu, P. and H. Murakami, 2022: “Climate variability and tropical cyclone activity.”
707 Cambridge University Press. 320 pp, doi:10.1017/9781108586467.

708 Delworth, T. L., and co-authors, 2006: GFDL’s CM2 global coupled climate models. Part I:
709 Formulation and simulation characteristics. *J. Climate*, **19**, 643–674,
710 doi:10.1175/JCLI3629.1.

711 Delworth, T. L., and co-authors, 2012: Simulated climate and climate change in the GFDL
712 CM2.5 high-resolution coupled climate model. *J. Climate*, **25**, 2755–2781,
713 doi:10.1175/JCLI-D-11-00316.1.

714 Delworth, T. L., and coauthors, 2020: SPEAR – the next generation GFDL modeling system
715 for seasonal to multidecadal prediction and projection. *J. Adv. Model. Earth Syst.*, **12**,
716 e2019MS001895, doi:10.1029/2019MS001895.

717 Emanuel, K. A., and Nolan, D. S., 2004: Tropical cyclone activity and global climate.
718 Preprints, 26th Conf. on Hurricanes and Tropical Meteorology, Miami, FL, Amer. Meteor.
719 Soc., 240–241.

720 Emanuel, K., 2005: Increasing destructiveness of tropical cyclones over the past 30 years.
721 *Nature*, **436**, 686–688, doi:10.1038/nature03906.

722 Emanuel, K., 2007: Environmental factors affecting tropical cyclone power dissipation. *J.*
723 *Climate*, **20**, 5497–5509, doi:10.1175/2007JCLI1571.1.

724 Gray W. M., 1984a: Atlantic seasonal hurricane frequency. Part I: El Nino and 30 mb quasi-
725 biennial oscillation influences. *Mon. Wea. Rev.*, **112**, 1649–1668, doi:10.1175/1520-
726 0493(1984)112<1649:ASHFPI>2.0.CO;2.

727 Gray W. M., 1984b: Atlantic seasonal hurricane frequency. Part II: Forecasting its variability.
728 *Mon. Wea. Rev.*, **112**, 1669–1683, doi: 10.1175/1520-
729 0493(1984)112<1669:ASHFPI>2.0.CO;2.

730 Goldenberg, S. B., L. J. Shapiro, 1996: Physical mechanisms for the association of El Niño
731 and west African rainfall with Atlantic major hurricane activity. *J. Climate*, **9**, 1169–1187,
732 doi:10.1175/1520-0442(1996)009<1169:PMFTAO>2.0.CO;2.

733 Harris, L.M, S.-J. Lin, and C.Y. Tu, 2016: High-resolution climate simulations using GFDL
734 HiRAM with a stretched global grid. *J. Climate*, **29**, 4293–4314, doi:10.1175/JCLI-D-15-
735 0389.1.

736 Jia, L., T. L. Delworth, S. Kapnick, X. Yang, N. Johnson, W. Cooke, F. Lu, M. Harrison, A.
737 Rosati, F. Zeng, C. McHugh, A. T. Wittenberg, L. Zhang, H. Murakami, and K. Tseng,
738 2022: Skilful seasonal prediction of North American summertime heat extremes. *J.*
739 *Climate*, **35**, 4331–4345, doi:10.1175/JCLI-D-21-0364.1.

740 Kim, H.-S., C.-H. Ho, J.-H. Kim, and P.-S. Chu, 2012: Track-pattern –based model for
741 seasonal prediction of tropical cyclone activity in the western North Pacific, *J. Climate*,
742 **25**, 4660–4678, doi:10.1175/JCLI-D-11-00236.1.

743 Kirtman, B. P., and Coauthors, 2014: The North American Multimodel Ensemble: Phase-1
744 Seasonal-to-Interannual Prediction; Phase-2 toward Developing Intraseasonal Prediction.
745 *Bull. Amer. Meteor. Soc.*, **95**, 585–601, doi:10.1175/BAMS-D-12-00050.1.

746 Knapp, K. R., M. C. Kruk, D. H. Levinson, H. J. Diamond, and C. J. Neumann (2010), The
747 international best track archive for climate stewardship (IBTrACS): Unifying tropical
748 cyclone best track data. *Bull. Amer. Meteor. Soc.*, **91**, 363–376,
749 doi:10.1175/2009BAMS2755.1.

750 Klotzbach, P.J., and W. M. Gray, 2009: Twenty-five years of Atlantic basin seasonal hurricane
751 forecasts (1984–2008). *Geophys. Res. Lett.*, **36**, L09711, doi:10.1029/2009GL037580.

752 Klotzbach, P. J., E. Blake, J. Camp, L. Caron, J. Chan, N. Kang, Y. Kuleshov, S. Lee, H.
753 Murakami, M. Saunders, Y. Takaya, F. Vitart, and R. Zhan, 2019: Seasonal Tropical
754 Cyclone Forecasting. *Trop. Cyclone Res. Rev.*, **8(3)**, 134–149,
755 doi:10.6057/2019TCRR03.03.

756 Kobayashi, S., and co-authors, 2015: The JRA-55 reanalysis: General specifications and basic
757 characteristics. *J. Meteor. Soc. Japan*, **93**, 5–48, doi:10.2151/jmsj.2015-001.

758 Kossin, J.P. and D.J. Vimont, 2007: More general framework for understanding Atlantic
759 hurricane variability and trends. *Bull. Amer. Meteor. Soc.*, **88**, 1767–1782,
760 doi:10.1175/BAMS-88-11-1767.

761 Krishnamurthy, L., G. A. Vecchi, R. Msadek, H. Murakami, A. Wittenberg, and F. Zeng, 2016:
762 Impact of strong ENSO on regional tropical cyclone activity in a high-resolution climate
763 model. *J. Climate*, **29**, 2375–2394, doi:10.1175/JCLI-D-15-0468.1.

764 LaRow, T. E., Y. –K. Lim, D. W. Shin, E. P. Chassignet, and S. Cocks, 2008: Atlantic basin
765 seasonal hurricane simulations. *J. Climate*, **21**, 3191–3206, doi:10.1175/2007JCLI2036.1.

766 LaRow, T. E., L. Stefanova, D. –W. Shin, and S. Cocks, 2010: Seasonal Atlantic tropical
767 cyclone hindcasting/forecasting using two sea surface temperature datasets. *Geophys. Res.
768 Lett.*, **37**, L02804, doi:10.1029/2009GL041459.

769 Li, X., S. Yang, H. Wang, X. Jia, and A. Kumar, 2013: A dynamical-statistical forecast model
770 for the annual frequency of western Pacific tropical cyclones based on the NCEP Climate
771 Forecast System version 2. *J. Geophys. Res.*, **118**, 12061–12074,
772 doi:10.1002/2013JD020708.

773 Liu, M., G. A. Vecchi, J. A. Smith, H. Murakami, R. Gudgel, and X. Yang, 2018: Towards
774 dynamical seasonal forecast of extratropical transition in the North Atlantic. *Geophys. Res.
775 Lett.*, **45**, 12602–12609, doi:10.1029/2018GL079451.

776 Lu, F., and Coauthors, 2020: GFDL’s SPEAR Seasonal Prediction System: Initialization and
777 Ocean Tendency Adjustment (OTA) for Coupled Model Predictions. *J. Adv. Model. Earth
778 Syst.*, **12**, e2020MS002, doi:10.1029/2020MS002149.

779 Maloney, E. D., and D. L. Hartmann, 2000: Modulation of hurricane activity in the Gulf of
780 Mexico by the Madden-Julian oscillation. *Science*, **287 (5460)**, 2002–2004,
781 doi:10.1126/science.287.5460.2002.

782 Murakami, H. and B. Wang, 2010: Future change of North Atlantic tropical cyclone tracks:
783 Projection by a 20-km-mesh global atmospheric model. *J. Climate*, **23**, 2699–2721,
784 doi:10.1175/2010JCLI3338.1.

785 Murakami, H., B. Wang, T. Li, and A. Kitoh, 2013: Projected increase in tropical cyclones
786 near Hawaii. *Nat. Clim. Change*, **3**, 749–754, doi:10.1038/nclimate1890.

787 Murakami, H., G. A. Vecchi, S. Underwood, T. L. Delworth, A. T. Wittenberg, W. G.
788 Anderson, J. -H. Chen, R. G. Gudgel, L. Harris, S. -J. Lin, and F. Zeng, 2015: Simulation
789 and prediction of Category 4 and 5 hurricanes in the high-resolution GFDL HiFLOR
790 coupled climate model. *J. Climate*, **28**, 9058–9079, doi:10.1175/JCLI-D-15-0216.1.

791 Murakami, H., G. A. Vecchi, G. Villarini, T. L. Delworth, R. Gudgel, S. Underwood, X. Yang,
792 W. Zhang, and S. Lin, 2016a: Seasonal forecasts of major hurricanes and landfalling
793 tropical cyclones using a high-resolution GFDL coupled climate model. *J. Climate*, **29**,
794 7977–7989, doi:10.1175/JCLI-D-16-0233.1.

795 Murakami, H., G. Villarini, G. A. Vecchi, W. Zhang, and R. Gudgel, 2016b: Statistical-
796 dynamical seasonal forecast of North Atlantic and U.S. landfalling tropical cyclones using
797 the high-resolution GFDL FLOR coupled model. *Mon. Wea. Rev.*, **144**, 2101–2123,
798 doi:10.1175/MWR-D-15-0308.1.

799 Murakami, H., G. A. Vecchi, T. L. Delworth, A. T. Wittenberg, S. Underwood, R. Gudgel, X.
800 Yang, L. Jia, F. Zeng, K. Paffendorf, and W. Zhang, 2017: Dominant role of subtropical
801 Pacific warming in extreme eastern Pacific hurricane seasons: 2015 and the future. *J.*
802 *Climate*, **30**, 243–264, doi:10.1175/JCLI-D-16-0424.1.

803 Murakami, H., E. Levin, T. L. Delworth, R. Gudgel, and P. -C. Hsu, 2018: Dominant effect of
804 relative tropical Atlantic warming on major hurricane occurrence. *Science*, **362**, 794–799,
805 doi:10.1126/science.aat6711.

806 Murakami, H. and B. Wang, 2022: Patterns and frequency of projected future tropical cyclone
807 genesis are governed by dynamic effects. *Commun. Earth Environ.*, **3**, 77,
808 doi:10.1038/s43247-022-00410-z.

809 Nasuno, T., M. Nakano, H. Murakami, K. Kikuchi, and Y. Yamada, 2022: Impacts of
810 midlatitude western North Pacific sea surface temperature anomaly on the subseasonal to
811 seasonal tropical cyclone activity: Case study of the 2018 boreal summer. *SOLA*, **18**, 88–
812 95, doi:10.2151/sola.2022-015.

813 Qian, Y., H. Murakami, M. Nakano, P. -C. Hsu, T. L. Delworth, S. B. Kapnick, V.
814 Ramaswamy, T. Mochizuki, Y. Morioka, T. Doi, T. Kataoka, T. Nasuno, and K. Yoshida,
815 2019: On the mechanisms of the active 2018 tropical cyclone season in the North Pacific.
816 *Geophys. Res. Lett.*, **46**, 12293–12302, doi:10.1029/2019GL084566.

817 Reynolds, R. W., N. A. Rayner, T. M. Smith, D.C. Stokes, and W. Wang, 2002: An improved in
818 situ and satellite SST analysis for climate. *J. Climate*, **15**, 1609–1625, doi:10.1175/1520-
819 0442(2002)015<1609:AIISAS>2.0.CO;2.

820 Siegel, S., and N. Castellan, 1988: "Nonparametric Statistics For The Behavioral Sciences",
821 McGraw-Hill, New York, 235-244, 399 pp.

822 Smith, D.M. and co-authors, 2010: Skilful multi-year predictions of Atlantic hurricane
823 frequency. *Nat. Geosci.*, **3**, 846–849, doi:10.1038/ngeo1004.

824 Takaya, Y., L. Caron, E. Blake, F. Bonnardotd, N. Bruneau, J. Camp, J. Chan, P. Gregory, J. J.
825 Jones, N. Kang, P. Klotzbach, Y. Kuleshov, J. Lockwood, H. Murakami, A. Nishimura, D.
826 R. Pattanaik, T. Philp, Y. Ruprich-Robert, R. Toumi, F. Vitart, S. Won, and R. Zhan, 2023:
827 Recent advances in seasonal and multi-annual tropical cyclone forecasting. *Trop. Cyclone*
828 *Res. Rev.*, **12**, 182–199, doi:10.1016/j.tcerr.2023.09.003.

829 Tseng, K., N. C. Johnson, S. B. Kapnick, T. L. Delworth, F. Lu, W. Cooke, A. T. Wittenberg,
830 A. J. Rosati, L. Zhang, C. McHugh, X. Yang, M. Harrison, F. Zeng, G. Zhang, H.
831 Murakami, M. Bushuk, and L. Jia, 2021: Are multiseasonal forecasts of atmospheric rivers
832 possible? *Geophys. Res. Lett.*, **48**, e2021GL094000, doi:10.1029/2021GL094000.

833 Vecchi, G. A., and co-authors, 2011: Statistical–dynamical predictions of seasonal North
834 Atlantic hurricane activity. *Mon. Wea. Rev.*, **139**, 1070–1082,
835 doi:10.1175/2010MWR3499.1.

836 Vecchi, G. A., and co-authors, 2014: On the seasonal forecasting of regional tropical cyclone
837 activity. *J. Climate*, **27**, 7994–8016, doi:10.1175/JCLI-D-14-00158.1.

838 Vecchi, G. A., and co-authors, 2019: Tropical cyclone sensitivities to CO₂ doubling: roles of
839 atmospheric resolution, synoptic variability and background climate changes. *Clim. Dyn.*,
840 **53(9-10)**, 5999–6033, doi:10.1007/s00382-019-04913-y.

841 Villarini, G., G. A. Vecchi, and J. A. Smith, 2010: Modeling of the dependence of tropical
842 storm counts in the North Atlantic basin on climate indices. *Mon. Wea. Rev.*, **138**, 2681–
843 2705

844 Vitart, F., and T. N. Stockdale, 2001: Seasonal forecasting of tropical storms using coupled
845 GCM integrations, *Mon. Wea. Rev.*, **129**, 2521–2537, doi:10.1175/1520-
846 0493(2001)129<2521:SFOTSU>2.0.CO;2.

847 Vitart, F., 2006: Seasonal forecasting of tropical storm frequency using a multi-model
848 ensemble. *Quart. J. Roy. Meteor. Soc.* **132**, 647–666, doi:10.1256/qj.05.65.

849 Vitart, F., and co-authors, 2007: Dynamically-based seasonal forecasts of Atlantic tropical
850 storm activity issued in June by EUROSIP. *Geophys. Res. Lett.*, **34**, L16815,
851 doi:10.1029/2007GL030740.

852 Wang, B. and H. Murakami, 2020: Dynamic genesis potential index for diagnosing present-
853 day and future global tropical cyclone genesis. *Environ. Res. Lett.*, **15**, 114008,
854 doi:10.1088/1748-9326/abbb01.

855 Wang, H., J.-K. E. Schemm, A. Kumar, W. Wang, L. Long, M. Chelliah, G.D. Bell, and P.
856 Peng, 2009: A Statistical Forecast Model for Atlantic Seasonal Hurricane Activity Based
857 on the NCEP Dynamical Seasonal Forecast. *J. Climate*, **22**, 4481–4500,
858 doi:10.1175/2009JCLI2753.1.

859 Wang, Z., G. Zhang, T. J. Dunkerton, and F. F. Jin, 2020: Summertime stationary waves
860 integrate tropical and extratropical impacts on tropical cyclone activity. *Proc. Natl. Acad.
861 Sci. USA*, 117, 22 720–22 726, doi:10.1073/pnas.2010547117.

862 Yang X., T.L. Delworth., L. Jia, J.C. Johnson, F. Lu., and C. McHugh, 2022: On the seasonal
863 prediction and predictability of winter surface temperature swing index over North
864 America. *Front. Clim.* **4**, 972119, doi:10.3389/fclim.2022.972119.

865 Zhang, S. and A. Rosati, 2010: An inflated ensemble filter for ocean data assimilation with a
866 biased coupled GCM. *Mon. Wea. Rev.*, **138**, 3905–3931, doi:10.1175/2010MWR3326.1.

867 Zhang, G., H. Murakami, R. Gudgel, and X. Yang, 2019: Dynamical seasonal prediction of
868 tropical cyclone activity: Robust assessment of prediction skill and predictability.
869 *Geophys. Res. Lett.*, 46, 5506–5515, doi:10.1029/2019GL082529.

870 Zhang, W., G. A. Vecchi, G. Villarini, H. Murakami, R. Gudgel, and X. Yang, 2017:
871 Statistical-dynamical seasonal forecast of Western North Pacific and East Asia landfalling
872 tropical cyclones using the GFDL FLOR Coupled Climate Model. *J. Climate*, 30, 2209–
873 2232, doi:10.1175/JCLI-D-16-0487.1.

874 Zhang, W., G. Villarini, G. A. Vecchi, and H. Murakami, 2019: Rainfall from Tropical
875 Cyclones: High-resolution Simulations and Seasonal Forecasts. *Clim. Dyn.*, **52(9-10)**,
876 5269–5289, doi:10.1007/s00382-018-4446-2.

877 Zhao, M., I. M. Held, and G. A. Vecchi, 2010: Retrospective forecasts of the hurricane season
878 using a global atmospheric model assuming persistence of SST anomalies. *Mon. Wea. Rev.*,
879 **138**, 3858–3868, doi:10.1175/2010MWR3366.1.

880 Zhao, M. and Coauthors, 2018: The GFDL global atmospheric and land model AM4.0/LM4.0
881 – Part I: Simulation characteristics with prescribed SSTs. *J. Adv. Model. Earth Syst.*, **10(3)**,
882 735–769, doi:10.1002/2017MS001208.